Crystal structure and transport properties of Ba8Ge43 3

Umut Aydemir, Christophe Candolfi, Horst Borrmann, Michael Baitinger, Alim Ormeci, Wilder Carrillo-Cabrera, Caroline Chubilleau, Bertrand Lenoir, Anne Dauscher, Niels Oeschler, et al.

▶ **To cite this version:**

Umut Aydemir, Christophe Candolfi, Horst Borrmann, Michael Baitinger, Alim Ormeci, et al.. Crystal structure and transport properties of Ba8Ge43 3. Dalton Transactions, 2010, 39 (4), pp.1078-1088. 10.1039/B919726E . hal-03997210

HAL Id: hal-03997210
https://hal.science/hal-03997210v1

Submitted on 20 Feb 2023

HAL is a multi-disciplinary open access archive for the deposit and dissemination of scientific research documents, whether they are published or not. The documents may come from teaching and research institutions in France or abroad, or from public or private research centers.

L'archive ouverte pluridisciplinaire **HAL**, est destinée au dépôt et à la diffusion de documents scientifiques de niveau recherche, publiés ou non, émanant des établissements d'enseignement et de recherche français ou étrangers, des laboratoires publics ou privés.

Crystal structure and transport properties of $Ba_8Ge_{43}\square_3$

U. Aydemir[1], C. Candolfi[1], H. Borrmann[1], M. Baitinger[1], A. Ormeci[1], W. Carrillo-Cabrera[1], C. Chubilleau[2], B. Lenoir[2], A. Dauscher[2], N. Oeschler[1], F. Steglich[1], Yu. Grin[1*]

[1]*Max-Planck-Institut für Chemische Physik fester Stoffe, Nöthnitzer Str. 40, 01187 Dresden, Germany*

[2]*Institut Jean Lamour, UMR CNRS-Nancy Université-UPVM 7198, Ecole Nationale Supérieure des Mines de Nancy, Parc de Saurupt, 54042 Nancy cedex, France*

*Corresponding author: grin@cpfs.mpg.de

Abstract

Single phase clathrate-I $Ba_8Ge_{43}\square_3$ (space group $Ia\bar{3}d$ (no. 230), a = 21.307(1) Å) was synthesized by use of a quenching technique. Specimens for physical property measurements were characterized by microstructure analysis and X-ray diffraction on polycrystalline samples as well as single crystals. Transport properties including thermopower, electrical resistivity, thermal conductivity and specific heat capacity were investigated in a temperature range of 2 - 673 K. The electrical resistivity exhibits a metal-like temperature dependence below 300 K turning into a semiconductor-like behaviour above 300 K. The analysis of the specific heat at low temperature indicates a finite density of states at the Fermi level, thus corroborating the metallic character below 300 K. The temperature dependence of the specific heat was modelled assuming Einstein-like localized vibrations of Ba atoms inside the cages of the Ge framework. A conventional crystal-like behaviour of the thermal conductivity with a low lattice contribution (κ_l(300 K) = 2.7 W m^{-1} K^{-1}) has been evidenced.

I. Introduction

Intermetallic clathrates have attracted attention because of their intriguing properties such as high thermoelectric efficiency in $Ba_8Ga_{16}Ge_{30}$ [1], glass-like characteristic of heat transport in $Sr_8Ga_{16}Ge_{30}$ [2] or superconductivity in $Na_2Ba_6Si_{46}$ [3]. It has been expected that these physical properties might be tuned by changing the composition but it turned out that the structure-property relations in clathrates are rather complex. The crystal structure of intermetallic clathrate-I compounds is characterized by a four-bonded anionic host framework of typically group 14 elements (Si, Ge, Sn), which may be substituted by either group 13 elements or transition metals. The host framework comprises space-filling polyhedral cages, which are occupied by electropositive guest atoms such as alkali metals, Sr, Ba or Eu [4]. Host-guest interaction of ionic nature implies transfer of valence electrons from guest atoms towards the framework. By partial substitution of group 14 elements with three-valent atoms like Ga, the additional electrons may be accommodated by formation of four-bonded Zintl-anions [(4b)Ga^-]. This typically results in clathrate phases like $K_8Ga_8Si_{38}$ [5] or $Ba_8Ga_{16}Ge_{30}$ [6] with the electronic balances $[K^+]_8[Ga^-]_8[Si^0]_{38}$ and $[Ba^{2+}]_8[Ga^-]_{16}[Ge^0]_{30}$, respectively. However, complete charge balance is not always achieved [7]. In particular clathrates with homoatomic framework of four-bonded group 14 atoms do not require any additional electrons if following the 8-*N* rule. Nevertheless, such compounds containing excess electrons are often observed. In the metallic clathrate-I silicides like Na_8Si_{46} [8] or $Cs_{8-x}Si_{46}$ [9], the electrons transferred from the guest atoms fill up antibonding conduction bands of the corresponding empty Si_{46} clathrate. Clathrates of the heavier homologues Ge and Sn may accommodate excess electrons also by the formation of defects. It was shown by *von Schnering* from single crystal X-ray diffraction data that the binary clathrates 'K_8Ge_{46}' and 'Cs_8Sn_{46}' exist at the compositions $K_8Ge_{44}\square_2$ [10], and $Cs_8Sn_{44}\square_2$ [11],, respectively. If a single atom is removed from a four-connected Ge network, the resulting vacancy □ is

surrounded by four unsaturated three-bonded Ge atoms. The unsaturated Ge atoms can reach close shell configuration [(3b)Ge^{-}] each by additional electrons transferred from the electropositive guest atoms to the framework. Therefore, by the formation of defects, the electrons transferred to the host framework occupy non-bonding instead of antibonding states. In case of $K_8Ge_{44}\square_2$ two vacancies $\square$ per unit cell are surrounded by 8 three-bonded Ge anions reaching closed shell configuration with the valence electrons from 8 K atoms. The electronic balance $[K^+]_8[\square(Ge^-)_4]_2[Ge^0]_{36}$ is achieved, which may explain the semiconductor-like behaviour observed for $K_8Ge_{44}\square_2$ [12]. However, in case of $Ba_8Ge_{43}\square_3$ [13-16] neither composition, nor crystal structure, nor transport behaviour could be explained by applying simple electron counting. A full transfer of valence electrons from 8 Ba atoms yields 16 excess electrons, but only 12 [(3b)Ge^{-}] anions are available. Although the composition $Ba_8Ge_{43}\square_3$ suggests 4 excess electrons per formula unit in antibonding states, $Ba_8Ge_{43}\square_3$ was reported to be a semiconductor. The discrepancy has been tentatively ascribed to defect ordering within the Ge framework that may result in modifications of the electronic band structure near the Fermi level [15]. While clathrate-I compounds usually crystallize in the space group $Pm\bar{3}n$ (no. 223), $Ba_8Ge_{43}\square_3$ crystallizes, due to an ordered defect arrangement with a $2 \times 2 \times 2$ supercell, in the space group $Ia\bar{3}d$ [13-17]. Similar supercells with partial defect ordering have been reported for the tin clathrates $M_8Sn_{44}\square_2$ (M = Rb [18], Cs [19]). So far, the implications of the supercell formation in clathrate-I compounds are not completely understood.

$Ba_8Ge_{43}\square_3$ is a high temperature phase and only recently we reported on the first preparation of single-phase, polycrystalline bulk samples by using a quenching technique [20]. In agreement with previous results we confirmed the semiconducting-like behaviour of $Ba_8Ge_{43}\square_3$ above room temperature [15], but found rather complex transport behaviour towards low temperatures. In this contribution we discuss crystal structure and defect ordering

in terms of the reaction conditions. The transport behaviour of single phase samples is analyzed in the 2 – 673 K temperature range and referred to former results. Chemical bonding in $Ba_8Ge_{43}\square_3$ is analyzed in the electron localizability approach [21].

II. Experimental details

Synthesis – The samples were synthesized in an argon-filled glove box (O_2 and $H_2O \leq 1$ ppm) with a one-step reaction. Stoichiometric mixtures of Ba (Chempur, 99.9% metals basis) and Ge pieces (Chempur, 99.9999% metals basis) were put in a glassy carbon crucible (∅ 12 mm, l = 12mm, Sigradur) and heated slowly with an induction furnace (Hüttinger, 5 kW, coil ∅ 40 mm, length 35 mm; IR-Pyrometer, Maurer) until the reactants were completely molten. The melt was then poured onto a polished stainless-steel plate and immediately sandwiched with a second plate. The cooling rate obtained this way was higher than 10^3K/sec. For annealing experiments, phase pure bulk pieces of $Ba_8Ge_{43}\square_3$ were placed into glassy carbon crucibles, sealed in Ta tubes and in turn jacketed in argon-filled quartz ampoules. After 30 d at 790 °C, the ampoules were quenched in water.

X-Ray powder diffraction – Phase analysis on powdered samples was performed with X-ray Guinier diffraction technique (Huber G670 camera, Cu $K\alpha_1$ radiation, λ = 1.540598 Å, graphite monochromator, $5° \leq 2\theta \leq 100°$, $\Delta 2\theta = 0.005°$). The reflection positions were determined by profile deconvolution and corrected with LaB_6 standard (NIST, a = 4.1569162(97) Å at 295.5 K). The unit cell parameters were calculated then from a least-squares refinement.

X-ray single crystal diffraction – For the structure determination, selected single crystals were fixed on top of glass capillaries with grease (Apiezon H). Single crystal data were collected with a rotating-anode diffractometer (RIGAKU Spider, Varimax optical system, Ag $K\alpha$ radiation, λ = 0.56087 Å). Absorption correction was performed with a multi-scan

procedure. Details concerning the data collection and structure refinement are given in table 1, the atomic coordinates and displacement parameters in tables 2 and 3, the interatomic distances in table 4.

Differential scanning calorimetry – DSC measurements were performed with a Netzsch DSC 404 C instrument. About 30 mg of samples were weighted in a glassy carbon crucible (∅ 4 mm, l = 6 mm, Sigradur G, HTW) and then sealed in Nb ampoules (∅ 5 mm, 600 mg). The system was heated under Ar atmosphere from room temperature to 1200 °C by applying various heating (cooling) rates from 0.1 to 10 °C /min.

Microstructure analysis – Samples were polished with discs of micrometer-sized diamond powders (6, 3, 0.25 μm) in paraffin and investigated with a Philips XL 30 Scanning Electron Microscope (LaB_6 cathode). Energy dispersive X-ray spectroscopy (EDXS) was performed with an attached EDAX Si (Li) detector. The composition of the clathrate phase was determined by wavelength dispersive X-ray spectroscopy (WDXS, Cameca SX 100) by using Ba_6Ge_{25} and α-Ge as Ba and Ge standards, respectively.

Sample preparation for physical properties – For transport property investigations, parallelepipeds of $1 \times 2 \times 8$ mm^3 were cut from the quenched sample with a diamond wire saw. A square-shaped sample of $6 \times 6 \times 1$ mm^3 was cut for the high temperature thermal diffusivity measurement.

Electrical resistivity – Measurements from 2 to 350 K were performed by a four-probe method using gold wires attached with a tiny amount of silver paste and the ac transport option of a PPMS (Quantum Design). The electrical resistivity in the 300 – 673 K temperature range was investigated using of a four-probe method (ZEM 3, Ulvac-Riko).

Thermopower and thermal conductivity – Measurements between 5 and 350 K were performed by using a PPMS with thermal transport option. Thermopower was measured simultaneously with electrical resistivity in the temperature range 300 – 673 K by using a

static dc method (ZEM 3, Ulvac-Riko).

Specific heat capacity – Measurements were carried out from 2 up to 300 K by a relaxation technique using a Quantum Design PPMS.

Thermal diffusivity – Thermal diffusivity a was measured by using a laser flash technique (Netzsch LFA 427) in argon atmosphere over the temperature range 300 K – 673 K. Thermal conductivity was then calculated via $\kappa(T) = a(T)\ \rho_{V,293K}\ C_{p,293K}$ where ρ_V and C_p are the density and specific heat at 293 K, respectively, which are considered as first approximation for the whole temperature range.

Calculation procedures – Electronic structure calculation and bonding analysis were carried out using the TB-LMTO-ASA program package [22]. The atomic coordinates for a structure model with fully ordered defects was taken from [14] (Space group $Ia\bar{3}d$, a = 21.3074(5) Å, Ba1 in 16(*a*) 0 0 0; Ba2 in 48(*g*) *x* 1/4+*x* 1/8, *x* = 0.2528; Ge11 in 24(*d*) 0 ¼ 3/8; Ge22 in 32(*e*) *xxx*, *x* = 0.09144; Ge21 in 96(*h*) *xyz*, *x* = 0.08999, *y* = 0.40513, *z* = 0.09097; Ge321 in 96(*h*) *xyz*, *x* = 0.49942, *y* = 0.15332, *z* = 0.05629; Ge322 in 96(*h*) *xyz*, *x* = 0.00111, *y* = 0.16667, *z* = 0.06549). The Barth-Hedin exchange potential [23] was employed for the LDA calculations. The radial scalar-relativistic Dirac equation was solved to get the partial waves. The calculation within the atomic sphere approximation (ASA) includes corrections for the neglect of interstitial regions and partial waves of higher order [24]. Nevertheless, the addition of empty spheres E was necessary at the positions of the framework defects and within the large cage around Ba2. The following radii of the atomic spheres were applied for the calculations: *r*(Ba1) = 2.451 Å, *r*(Ba2) = 2.419 Å, *r*(Ge11) = 1.470 Å, *r*(Ge22) = 1.436 Å, *r*(Ge21) = 1.415 Å, *r*(Ge321) = 1.460 Å, *r*(Ge322) = 1.519 Å, *r*(E1) = 1.021 Å, *r*(E2) = 1.018 Å, *r*(E3) = 1.019 Å, *r*(E4) = 0.957 Å. A basis set containing Ba(6*s*, 5*d*) and Ge(4*s*, 4*p*) orbitals was employed for a self-consistent calculation with Ba(6*p*, 4*f*) and Ge(4*d*) functions being downfolded.

The electron localizability indicator (ELI, Υ) [25] was evaluated in the ELI-D representation [26] with an ELI-D module within the TB–LMTO–ASA program package. ELI-D and electron density were analyzed using the program Basin [27] with consecutive integration of the electron density in basins, which are bound by zero-flux surfaces in the ELI-D or electron density gradient field. Such treatment of ELI-D is similar to the procedure proposed by Bader for the electron density [28].

III. Results and discussion

A. Preparation of $Ba_8Ge_{43}\square_3$

$Ba_8Ge_{43}\square_3$ forms on cooling at 810 °C by a peritectic reaction from α-Ge and melt and crystallizes at 808 °C in an eutectic mixture with Ba_6Ge_{25}. $Ba_8Ge_{43}\square_3$ is a high temperature phase thermodynamically stable in the temperature range 770 °C – 810 °C [14]. At temperatures slightly lower than 770 °C, $Ba_8Ge_{43}\square_3$ decomposes rapidly to Ba_6Ge_{25} and α-Ge. Cooling rates applied to samples by water quenching of reaction ampoules have been insufficient to suppress the partial decomposition. We prepared single phase $Ba_8Ge_{43}\square_3$ by quenching of melt between cold steel plates. Samples were typically obtained as metallic grey disks of 10 mm in diameter and 1 mm in thickness. The product is stable in air as well as in diluted acids and did not show any impurity phase in XRPD (Fig. 1). Microstructure investigations confirmed the presence of only the target clathrate phase (Fig. 2a). After further annealing in closed ampoules, the formerly phase pure bulk samples partially decomposed on cooling to α-Ge and Ba_6Ge_{25} (Fig. 1, 2b). The clathrate composition $Ba_{8.0(1)}Ge_{43.0(1)}$ as determined from WDX as well as the lattice parameter a = 21.307(1) Å did not change significantly on annealing (Tab. 5). A homogeneity range was not found within the detection limit of XRPD and WDXS as well as lattice parameter determination.

B. Crystal structure and chemical bonding in $Ba_8Ge_{43}\square_3$

Similarly to the diamond structure of α-Ge, a hypothetical clathrate-I germanium Ge_{46} consists of four-connected Ge atoms. In contrast to the puckered hexagons in α-Ge, the Ge atoms in the clathrate-I allotrope form pentagons and planar hexagons. The crystal structure in the space group $Pm\bar{3}n$ (no. 223) represents a space filling stacking of polyhedrons, namely dodecahedra Ge_{20} $[5^{12}]$ and tetrakaidecahedra Ge_{24} $[5^{12}6^2]$, with the Ge sites 6*c* (Ge1), 16*i* (Ge2) and 24*k* (Ge3). In the intermetallic germanium clathrates both polyhedral cages host electropositive metal atoms at the sites 2*a* (*M*1@Ge_{20}) and 6*d* (*M*2@Ge_{24}), respectively (Fig. 3).

Although often stated, not all of the framework atoms in clathrate-I structure have an ideal tetrahedral environment. In fact, the 120° angles of the planar hexagons formed by Ge1 and Ge3 are unfavourable for (4b)Ge atoms. The bond angles of Ge1 atoms joining two such hexagons are especially unfavourable and consequently, vacancies in clathrate-I compounds are usually formed at this position. The hexagons are connected via common Ge1 atoms to infinite chains along [100] direction, in which every second hexagon is rotated by 90° (Fig. 4a). The formation of vacancies at the Ge1 site leads also to a release of tension, which is expressed by the relaxation of the neighbouring Ge3 atoms, shifted towards the vacancy by about 0.3 Å [14]. The presence of 2 vacancies in the same 6-ring is not expected, because a full relaxation of neighbouring Ge3 atoms would lead to a large elongation of Ge3–Ge3 bonds as well as direct contact of [(3b)Ge^-] anions (Fig. 4b). Thus, the Ge1 position at 6*c* should not be emptied by more than 50 %, which may explain, why the composition $Ba_8Ge_{43}\square_3$ with four excess electrons is formed instead of '$Ba_8Ge_{42}\square_4$' with complete electron balance. Crystal structure determinations of $Ba_8Ge_{43}\square_3$ are in accord with the considerations above. The compound has been first obtained with space group $Pm\bar{3}n$ and apparently statistical defect distribution [13]. Later on, superstructures in the space group $Ia\bar{3}d$ have been

identified with partially-ordered defect arrangement after fast cooling and almost fully-ordered defect arrangement after annealing at 795°C [14]. Compared with the ideal clathrate-I type crystal structure with space group $Pm\bar{3}n$ and the cubic cell parameter a_0, in the observed superstructure with $a = 2\ a_0$ of the direct subgroup $Ia\bar{3}d$ a site splitting according to Fig. 5 is observed.

To investigate the effect of temperature treatment on defect ordering, we performed additional structure determinations on two single crystals obtained from steel quenching without and with subsequent annealing. For a fully-ordered structure in the space group $Ia\bar{3}d$ either the site Ge11 or Ge12 should be empty, for partially-ordered defects both positions are differently occupied. For both crystals, we found that the position Ge11 is much more occupied (occ. > 90%) than Ge12 (occ. < 10%). The disorder in the annealed sample is even slightly higher. Thus, both preparation techniques yield only partial ordering of the defects in the framework (Tables 2, 3) and a fully-ordered structure was not obtained. Refinement of the occupancy factors for all partially occupied positions gave the same composition $Ba_8Ge_{43.0(1)}$ for crystals of both quenched and annealed samples (Table 2, 4). Hence, the chemical composition does not depend on the thermal treatment and is in agreement with previous reports.

From the experimental results the question arises, why the superstructure of $Ba_8Ge_{43}\square_3$ is formed even after rapid quenching. We assume that the preferred superstructure formation in $Ba_8Ge_{43}\square_3$ is related to the local distortion of the framework positions by defect formation: In a type-I clathrate compound without framework defects in space group $Pm\bar{3}n$, the spiro-chain of hexagons along [100] consists of the positions Ge1 and Ge3 (Fig. 6a). A defect on position Ge1 induces a distinct shift of the neighbouring Ge3 atoms as discussed above. As long as the defects are statistically distributed over the Ge1 site, the crystal structure still belongs to space group $Pm\bar{3}n$ (Fig. 6b). The presence of defects on position Ge1 is expressed in diffraction experiments first of all by a lowered occupancy of the Ge1 site. Furthermore, as

the Ge1 position is surrounded by four Ge3 positions, the shift of Ge3 atoms toward the defect results in two split positions Ge31 and Ge32. In diffraction experiments, the cubic translation symmetry may disguise local disorder such as partially occupied sites. If the diffraction data quality is not sufficient to resolve split sites for Ge3, a characteristic anisotropy of the thermal displacement parameters is observed for this position due to the superposition of two different sites. On the other hand, if the resolution from the diffraction experiment is sufficient, the occupancy of the split sites may be refined. It was shown for $Cs_8Sn_{44}\square_2$ that the occupancy of site Sn1 (occ ≈ 66 %) is directly correlated with the occupancies of the neighbouring split sites Sn31 (occ. ≈ 33 %) and Sn32 (occ. ≈ 66 %) [11]. Therefore, the occupancies of the split positions constitute a valuable tool to analyze the defect concentration especially in $Ba_8TM_xGe_{46-y}\square_{x+y}$ (*TM* = transition metal) clathrates [29].

According to the crystal structure refinement on annealed and quenched samples the position Ge311 with site symmetry $\bar{4}$ is occupied by SOF ~ 0.9 whereas the position Ge321 with site symmetry 222 is emptied to SOF ~0.1 (Tables 2,3) The partial occupancy of both positions might on the first look imply the presence of cumulated defects within the same hexagon, which would contradict the suggested boundary condition. However, the partial occupancy of the positions Ge11 and Ge12 (as well as Ge311, Ge312, Ge321 and Ge322) can be also a consequence of the positional disorder between neighbouring spiro-hexagon chains. A partial structure of these chains constitutes a 3D rod packing (Fig 7). If, e.g., one out of twelve rods is shifted so that atoms, formerly located at site Ge11, superimpose positions of site Ge12, a partial occupancy of 0.88 for Ge11, Ge311 and Ge321 and a partial occupancy of 0.12 for Ge12, Ge312 and Ge322 would result, which is quite close to the experimental occupancies (Tables 2 and 3). The breaking of the translational symmetry is in such case so weak that it would be hardly detected from diffraction data.

The formation of electron pairs, either in $2e^-$ bonds or lone pairs, is the key element of the

models for chemical bonding in clathrates. This opens a possibility to discover and visualize the chemical bonding using quantum chemical functions or functionals related to the correlated motion of electrons and electron pair density. The maxima of ELI in the valence region or/and structuring of the outer core shell provide signatures for directed covalent bonding. Analysis of the topology of ELI in vicinity of the defects in the hexagons for $Ba_8Ge_{43}\square_3$ (Fig. 4c) reveals maxima close to the mid points of Ge-Ge contacts within the framework. For both types of the Ge–Ge bonds, (3b)Ge-(4b)Ge and (4b)Ge-(4b)Ge, the topology of ELI reveals two-centre interactions. In addition, the maxima of ELI were found close to the (3b)Ge atom toward the defect position in the framework. They represent the 'lone' pairs. Integration of electron density yields 1.8 – 2.1 electrons within the basins of the bonding attractors and 1.8 – 2.0 electrons for the 'lone-pair' attractors. Thus, the ELI picture fits completely the expectations from the simple electron counting described above.

C. Electrical properties

The temperature dependence of the electrical resistivity was investigated in the 5 – 673 K temperature range (Fig. 8). The measured values are one order of magnitude lower than those previously reported [15] indicating the high quality of the present polycrystalline sample. At low temperatures the electrical resistivity displays a 'bad metal' behaviour ($\partial\rho / \partial T > 0$). Above room temperature, the resistivity turns into a semiconducting-like regime of conduction ($\partial\rho / \partial T < 0$). A gap of ≈ 60 meV might be inferred from an Arrhenius plot of the electrical resistivity in the 400 – 673 K temperature range. The high-temperature semiconducting-like behaviour is in agreement with the observations of Okamoto et al. [15]. The large intrinsic resistivity of $Ba_8Ge_{43}\square_3$ may be in particular caused by electronic correlations. The calculation of the electronic DOS for a fully ordered model of the crystal structure of $Ba_8Ge_{43}\square_3$ (cf. Experimental details) discloses a general picture as expected from

the electron counting above (Fig. 9, top): the bonding states at low energies are completely occupied (–12 eV < E <–0.8 eV). In addition, a part of the antibonding states (–0.5 eV < $E \leq E_F$) is filled by the excess electrons. A more detailed analysis of this part of electronic DOS reveals the position of the Fermi level on the steep shoulder (∂DOS/∂E < 0) of a spike (Fig. 9, middle). Such a picture resembles the electronic DOS for the strongly correlated systems, whereas the height of the spike in the DOS for $Ba_8Ge_{43}\square_3$ is much lower than usually observed for strongly correlated systems. With the enhanced volume of 15% we modelled roughly the temperature influence on the electronic structure. Under such conditions, the Fermi level is moving to the other side of the spike and shows now a positive gradient of DOS (∂DOS/∂E > 0, Fig. 9, bottom). A crossover between both positions of the Fermi level at the intermediate temperature is obvious.

Further experimental evidence for this changeover is provided by the temperature dependence of the thermopower (Fig. 10). While below 300 K the thermopower values are of the order of several μV K^{-1}, the thermopower linearly increases above this temperature to reach ≈ -40 μV K^{-1} at 673 K. The sign change in $S(T)$ around room temperature correlates with the position of the electrical resistivity maximum. However, the overall temperature dependence constitutes a striking and peculiar feature of the carrier transport in this compound. A complex behaviour emerges from these data: a low-temperature *n*-type conduction turning into *p*-type behaviour near 90 K that switches over to *n*-type conduction near room temperature and finally followed by a semiconductor-like behaviour up to 673 K. In non-magnetic materials, the thermopower mainly originates from the thermal diffusion of charge carriers. At low temperatures, an additional contribution may arise from phonon drag that leads to a maximum between $\theta_D/10$ and $\theta_D/3$. In the present case, a phonon-drag contribution may therefore manifest itself in the ≈ 25 – 75 K temperature range and account for the observed low-temperature maximum near 40 K. However, the lack of coincidence of this last temperature

with that of the maximum of the lattice thermal conductivity (see Section C) rather suggests an electronic origin. As it is shown from the band structure, the Fermi level is positioned in a region where strong variations of the density of states occur. As the temperature increases, a slight shift of the Fermi level may result in sign change of the energy derivative of the density of states, then leading to a crossover from *n*-type to *p*-type conduction. Thus, the two observed thermopower crossovers might reflect variations of the density of states near the Fermi level, as it is shown above for the calculated electronic DOS. Alternatively to this scenario, such complex behaviour may testify the breakdown of a single-band model that usually holds in ordinary metals, thus suggesting multi-band conduction with differing temperature-dependent mobilities of holes and electrons. In this regard, Hall effect as well as electron spectroscopy experiments are currently in progress to definitively settle this issue.

D. Thermal properties

Figure 11a shows the temperature dependence of the specific heat in the 2-300 K temperature range. At room temperature, the specific heat values are slightly larger than the Dulong-Petit law. Figure 11b illustrates the low-temperature dependence of the specific heat plotted as C_P/T vs T^2. A fit to the data following the conventional $C_p / T = \gamma + \beta T^2$ relation in the 2 - 4 K temperature range, where γ is the Sommerfeld coefficient standing for the electronic contribution and βT^2 the lattice contribution, leads to 24.8 mJ mol^{-1} K^{-2} and 0.79 mJ mol^{-1} K^{-4} for γ and β, respectively. The low but finite value of the Sommerfeld coefficient (0.5 mJ mol^{-1} K^{-1} atom^{-1}) confirms the existence of a Fermi surface, which appears consistent with both our low temperature measurements and band structure calculations. Assuming validity of the simple relation in the non-interacting limit γ = 0.173 N(E_F) (γ and N(E_F) are expressed in mJ mol^{-1} K^{-2} and states Ry^{-1}, respectively), the above-mentioned value leads to N(E_F) ≈ 143 states Ry^{-1} i.e. 10.5 states eV^{-1} per formula unit, in agreement with

our calculations. Previous theoretical studies on the hypothetic Ba_8Ge_{46} compound and on $Ba_8Ge_{43}\square_3$ within a model considering a non-ordered vacancy sublattice have led to N(E_F) values of ≈ 45 states eV^{-1} and ≈ 20 states eV^{-1}, respectively [30]. Both, these and our theoretical results show that vacancy ordering strongly reduces N(E_F), which may be a reason for the absence of superconductivity in $Ba_8Ge_{43}\square_3$ with respect to the Si-based counterpart [31-32]. This also underlines the importance of the superstructure for the transport properties in the present case. The β coefficient corresponds to an initial Debye-temperature of $\theta_D \sim 232\,\mathrm{K}$, in agreement with the values observed for several $Ba_8Ge_{43}\square_3$ - related compounds [33, 34].

A conventional description of the low temperature specific heat only applies in a narrow temperature window suggesting a complex phonon spectrum. This picture is reinforced by the overall temperature dependence of the lattice specific heat that cannot be solely described within the Debye theory in any extended temperature range. To have a deeper insight into the lattice dynamics of clathrate compounds, the specific heat is usually treated as a sum of a background vibrations spectrum originating from the cage-like structure i.e. a Debye contribution and of an Einstein contribution arising from the localized vibrational modes of the Ba atoms and quantified through characteristic Einstein temperatures, θ_E . The specific heat can be thus written as

$$C_p = C_{elec} + C_D + C_{Ei} = \gamma T + \frac{12\pi^4 N_D k_B}{5}\int \frac{x^4 e^x dx}{(e^x - 1)^2} + \sum_i p_i N_{Ei} R\left(\frac{\theta_{Ei}}{T}\right)^2 \frac{e^{\theta_{Ei}/T}}{(e^{\theta_{Ei}/T} - 1)^2} \qquad (1)$$

where $C_{elec} = \gamma T$ is the electronic contribution, C_D the lattice specific heat described within the Debye model and C_{Ei} the Einstein contribution of the i^{th} vibrational mode of the rattling atoms. In equation (1), $x = \hbar\omega / k_B T$ with $\hbar$ the reduced Planck constant and k_B the Boltzmann constant, N_D is the number of Debye oscillators per formula unit and p_i , N_{Ei}

and θ_{Ei} are the degrees of freedom, the number of Einstein oscillators, and the Einstein temperature related to the i^{th} vibrational mode, respectively. To emphasize this last contribution on the specific heat data, we have plotted C_p/T^3 as a function of T after subtraction of the electronic contribution (Figure 11c). The contribution of the localized vibrations then appears as a pronounced peak over a Debye background centred at ~ 10 K. To further analyze these localized modes, we used a model that takes into account the essential crystallographic characteristics of these compounds [35-36]. Several X-ray and neutron diffraction investigations have shown that the Ba2 atoms display large atomic displacement parameters (ADP) while the ADP values inferred for the Ba1 atoms are similar to those of the framework atoms [33]. Thus, only the Ba2 atoms can be considered to behave as Einstein-like oscillators. In addition, these atoms display anisotropic vibrations which require two vibrational modes to describe the two-dimensional in-plane (parallel to two hexagons, $\theta_{E2}^{||}$) and one-dimensional out-of-plane (θ_{E2}) motions. The degrees of freedom and the numbers of oscillators are then constrained and equal to $p_2^{||}N_{E2}^{||} = 2 \times 6$ and $p_2 N_{E2} = 1 \times 6$. The best fit to the data according to the relation $C_{E_i} = \sum_i p_i N_{Ei} R \left(\frac{\theta_{Ei}}{T}\right)^2 \frac{e^{\theta_{Ei}/T}}{(e^{\theta_{Ei}/T} - 1)^2}$ is shown in Figure 11c and results in $\theta_{E2}^{||} \approx 55$ K and $\theta_{E2} \approx 90$ K, consistent with larger in-plane vibrations amplitude which implies a lower Einstein temperature. The obtained values are also in good agreement with those obtained from the temperature dependence of the ADP values in several systems based on $Ba_8Ge_{43}\square_3$ [33, 34]. As can be appreciated in Figure 11c, this model provides a satisfying theoretical background to account for the low-temperature lattice specific heat of this compound. A Raman experiment revealed low-wavenumber peaks centred at 39, 46 and 68 cm^{-1} which were attributed to the motion of B atoms [37]. Though a specific heat analysis is not sensitive enough to probe fine details of the phonon spectrum as

compared to Raman spectroscopy or inelastic neutron scattering, the above-mentioned values appear in excellent agreement with these previous investigations (55 and 90 K results in 38 and 63 cm^{-1}, respectively).

Figure 12 shows the temperature dependence of the total thermal conductivity at low and high temperatures, respectively. Note that due to radiation losses inherent to the method used, the thermal conductivity has only been investigated up to 150 K in this setup. The measured values are coherent with those reported for the ternary $Ba_8M_xGe_{46-x-y}\square_y$ compounds [33, 34]. Using the measured thermal conductivity and electrical resistivity values and the Wiedemann-Franz law ($\lambda_e = LT/\rho$ with L the Lorenz number assumed to be equal to the value for a degenerate electron gas, $L = L_0 = 2.44 \times 10^{-8}$ V^2 K^{-2}), the lattice and electronic contributions may be separated from the total thermal conductivity (Figure 12b). At low temperatures, the electronic contribution only amounts to ≈ 1 % of the total thermal conductivity, which is therefore dominated by the lattice contribution. At high temperatures, the increase of λ is intimately related to the increase of the electrical resistivity. In the whole temperature range investigated, the lattice thermal conductivity values are small and in line with the data previously reported for Ge-based type-I clathrate compounds [33, 34]. An essential outcome of these measurements lies in the sharp maximum characteristic for crystalline lattices which contrasts with the glass-like behaviour observed, e.g., in *p*-type $Ba_8Ga_{16}Ge_{30}$, in $Eu_8Ga_{16}Ge_{30}$ or in $Sr_8Ga_{16}Ge_{30}$ [2, 38-40]. This result also seems to contradict the behaviour observed in the $Ba_8TM_xGe_{46-x-y}\square_y$ compounds for which a marked decrease of the sharp maximum occurs when x decreases i.e. when the vacancy concentration increases suggesting that phonon scattering on vacancies is the most prominent scattering mechanism at play [33].

Our result might indicate a more complex behaviour of the thermal transport in these materials upon alloying. As already mentioned, Ge substitution by transition elements drastically affect the vacancy ordering. If low substitution levels keep the vacancy sublattice

ordered, higher *M* content leads to a disordered arrangement. However, even low *M* content affects the superstructure which is then characterized by distorted polyhedra as a result of the decrease of the vacancy concentration. Therefore, these distortions may likely influence the thermal transport through enhanced disorder and may explain the much lower dielectric maximum observed. The highly ordered structure displayed by $Ba_8Ge_{43}\square_3$ may then be synonym of a lower degree of disorder consistent with a higher dielectric maximum. An alternative origin may be related to microstructural differences and/or to a small amount secondary phases displayed by the Ge-substituted samples.

Thermal transport measurements carried out on annealed samples of $Ba_8Ge_{43}\square_3$ seem to lend support for this second scenario. After annealing $Ba_8Ge_{43}\square_3$ samples contain small amounts of α-Ge and Ba_6Ge_{25}. Thermal conductivity measurements then clearly reveal a strong decrease of the dielectric maximum.

Based on the electrical resistivity, thermopower and thermal conductivity values, the maximum value of $ZT \approx 0.035$ at 673 K remains very low, as expected from the observed small thermopower values.

Conclusions

Single phase polycrystalline $Ba_8Ge_{43}\square_3$ samples have been synthesized by a quenching technique and carefully investigated to identify the vacancy ordering and to shed light on the relationship between the composition, the crystal structure and the physical properties. Structural and chemical characterizations have further corroborated the absence of secondary phases. Single crystal X-ray diffraction experiments enabled a thorough study of the crystal structure of this compound and, within some basic crystallographic considerations, a model of the vacancy ordering has been suggested providing a possible explanation for the presence of three vacancies per formula unit in this compound.

Transport properties including electrical resistivity, thermopower, thermal conductivity and heat capacity have been measured in a 2 – 673 K temperature range. The electrical properties reflect a metallic-like regime of conduction turning into a semiconductor-like behaviour near room temperature. Two crossovers from electronic to hole-like transport characterize the complex temperature dependence of the thermopower. Thermal transport measurements revealed a crystal-like behaviour of the lattice thermal conductivity that displays low values up to high temperature. Additional valuable information on the phonon spectrum of this material was provided by a detailed analysis of the temperature dependence of the specific heat capacity within the framework of the Debye model including Einstein-like modes. The obtained values of the characteristic Einstein temperatures associated to the Ba2 atoms motion are in excellent agreement with the low energy phonon modes experimentally observed by Raman spectroscopy. All these results underscore the complexity of this material and constitute a first and important step toward a unified picture of the subtle relationship between its structural and electronic properties.

Acknowledgement

Thanks are due to Petra Scheppan and Renate Hempel-Weber and members of the Kompetenzgruppe Struktur for providing experimental support.

Table 1: Crystallographic data for $Ba_8Ge_{43}\square_3$.

	Quenched	**Annealed**
Formula; molar mass	Ba_8Ge_{43}; 4220.85 g mol^{-1}	Ba_8Ge_{43}; 4220.85 g mol^{-1}
Crystal system; space group	Cubic; $I\,a\,\bar{3}\,d$ (no. 230)	Cubic; $I\,a\,\bar{3}\,d$ (no. 230)
***a* / Å, number of reflections**	21.3079(2), 112	21.3069(3), 112
Unit cell volume	9674.4(3) Å^3	9673.0(4) Å^3
***Z*; ρ_{calc}/(g cm^{-3})**	8; 5.7938(2)	8; 5.7946(2)
Diffractometer	RIGAKU Spider	RIGAKU Spider
λ / Å; monochromator	0.56087; multilayer-optics	0.56087; multilayer-optics
Crystal size	40 × 60 × 100 µm^3	20 × 80 × 120 µm^3
***T* / K**	295	295
***θ* range**	2.8° to 30.1°	2.8° to 34.2°
Indexes ranges	$-38 \le h \le 21$, $-38 \le k \le 38$, $-37 \le l \le 34$	$-24 \le h \le 41$, $-27 \le k \le 42$, $-32 \le l \le 41$
***μ* / mm^{-1}**	18.01	18.01
***F*(000) / e**	14590.6	14590.6
Absorption correction	Multi-scan	Multi-scan
Reflections collected; unique	42422; 2430 [R_{int} = 0.028]	50859; 3409 [R_{int} = 0.051]
Refined parameters	51	50
Refinement method	Full-matrix least-squares on F and F^2	Full-matrix least-squares on F and F^2
***R*(*F*), *R*(F^2) [I > 4σ(I)]**	0.0304, 0.0210	0.0668, 0.0609
Goodness-of-fit on *F*	1.01	1.01

Table 2: Atomic coordinates and displacement parameters (in Å^2) for $Ba_8Ge_{43}\square_3$ (quenched).

Atom	Site	*x*	*y*	*z*	U_{eq}	SOF
Ba1	16*a*	0	0	0	0.01082(4)	1.0
Ba2	48*g*	0.125	0.24755(2)	0.00245(2)	0.02867(8)	1.0
Ge11	24*d*	0.375	0	0.25	0.01266(2)	0.94(1)
Ge12	24*c*	0.125	0	0.25	0.012(2)*	0.06(1)
Ge21	32*e*	0.09149(2)	0.09149(2)	0.09149(2)	0.01237(7)	1.0
Ge22	96*h*	0.15546(2)	0.34015(2)	0.15900(2)	0.01199(1)	1.0
Ge311	96*h*	0.09666(3)	0.24949(3)	0.30634(3)	0.01219(1)	0.94(1)
Ge312	96*h*	0.0821(4)	0.2488(5)	0.3168(5)	0.013(2) *	0.06(1)
Ge321	96*h*	0.00093(3	0.16674(4)	0.06541(3)	0.01591(1)	0.94(1)
Ge322	96*h*	0.0010(6)	0.1535(5)	0.0552(5)	0.015(2) *	0.06(1)

* Uiso

Atom	U_{11}	U_{22}	U_{33}	U_{12}	U_{13}	U_{23}
Ba1	0.01082(7)	0.01082(7)	0.01082(7)	0.00017(1)	0.00017(1)	0.00017(1)
Ba2	0.0195(2)	0.03326(1)	0.03326(1)	–0.00185(1)	–0.00185(1)	–0.0027(2)
Ge11	0.0137(3)	0.0121(2)	0.0121(2)	0	0	0
Ge21	0.01237(1)	0.01237(1)	0.01237(1)	–0.00163(1)	–0.00163(1)	–0.00163(1)
Ge22	0.0122(2)	0.0121(2)	0.0117(2)	0.00191(1)	–0.00130(1)	0.00165(1)
Ge311	0.0113(2)	0.0125(2)	0.0127(2)	0.0003(2)	0.0010(2)	0.0003(2)
Ge321	0.0144(2)	0.0163(3)	0.0170(3)	–0.0005(2)	0.0005(2)	0.0023(2)

U_{eq} is defined as one third of the trace of the orthogonalized U_{ij} tensor, which is exp $(-2\pi^2 [h^2 a^{*2} U_{11} + ... + 2\ h\ k\ a^*\ b^*\ U_{12}])$

Table 3: Atomic coordinates and displacement parameters (in Å^2) for $Ba_8Ge_{43}\square_3$ (annealed).

Atom	Site	*x*	*y*	*z*	U_{eq}	SOF
Ba1	16*a*	0	0	0	0.01207(6)	1.0
Ba2	48*g*	0.125	0.24773(3)	0.00227(3)	0.03088(1)	1.0
Ge11	24*d*	0.375	0	0.25	0.0135(2)	0.91(1)
Ge12	24*c*	0.125	0	0.25	0.012(2)*	0.09(1)
Ge21	32*e*	0.09150(3)	0.09150(3)	0.09150(3)	0.01339(1)	1.0
Ge22	96*h*	0.15562(3)	0.34021(3)	0.15895(3)	0.01340(1)	1.0
Ge311	96*h*	0.09661(4)	0.24951(4)	0.30637(4)	0.0130(2)	0.91(1)
Ge312	96*h*	0.0814(5)	0.2490(6)	0.3170(5)	0.017(2)*	0.09(1)
Ge321	96*h*	0.00091(5)	0.16668(5)	0.06536(5)	0.0170(2)	0.91(1)
Ge322	96*h*	0.0004(6)	0.1528(5)	0.0554(5)	0.016(2)*	0.09(1)

Atom	U_{11}	U_{22}	U_{33}	U_{12}	U_{13}	U_{23}
Ba1	0.01207(1)	0.01207(1)	0.01207(1)	0.00034(1)	0.00034(1)	0.00034(1)
Ba2	0.0210(3)	0.0358(2)	0.0358(2)	–0.0016(2)	–0.0016(2)	–0.0030(3)
Ge11	0.0141(5)	0.0132(3)	0.0132(3)	0	0	0
Ge21	0.0134(2)	0.0134(2)	0.0134(2)	–0.0018(2)	–0.0018(2)	–0.0018(2)
Ge22	0.0133(2)	0.0134(3)	0.0135(3)	0.0023(2)	–0.0014(2)	0.0018(2)
Ge311	0.0120(3)	0.0133(3)	0.0137(3)	–0.0000(3)	0.0006(3)	0.0004(2)
Ge321	0.0156(3)	0.0171(4)	0.0184(4)	–0.0003(3)	0.0007(3)	0.0025(3)

Table 4: Interatomic distances for $Ba_8Ge_{43}\square_3$.

Atoms			*d* / Å (quenched)	*d* / Å (annealed)
Ba1	– Ge21	2 ×	3.3765(4)	3.3767(7)
	– Ge22	6 ×	3.3923(5)	3.3914(7)
	– Ge322	6 ×	3.476(11)	3.463(11)
	– Ge311	6 ×	3.4809(6)	3.4820(9)
	– Ge321	6 ×	3.8165(7)	3.815(1)
	– Ge312	6 ×	3.852(10)	3.865(11)
Ba2	– Ge321	2 ×	3.4284(8)	3.432(1)
	– Ge312	2 ×	3.466(10)	3.464(12)
	– Ge322	2 ×	3.502(13)	3.525(13)
	– Ge321	2 ×	3.5122(8)	3.511(1)
	– Ge311	2 ×	3.5547(7)	3.555(1)
	– Ge312	2 ×	3.557(10)	3.545(12)
	– Ge322	2 ×	3.594(13)	3.594(13)
	– Ge311	2 ×	3.6306(7)	3.626(1)
	– Ge12	2 ×	3.7304(3)	3.7328(5)
	– Ge11	2 ×	3.8041(3)	3.8012(5)
	– Ge21	2 ×	3.8946(6)	3.899(1)
	– Ge11	2 ×	3.8041(3)	3.930(1)
	– Ge22	2 ×	3.9285(6)	3.9285(6)
	– Ge22	2 ×	3.9296(6)	3.931(1)
	– Ge321	2 ×	3.9819(8)	3.986(1)
	– Ge312	2 ×	4.060(10)	4.057(11)
	– Ge22	2 ×	4.0932(6)	4.085(1)
Ge11	– Ge312	4 ×	2.143(10)	2.131(11)
	– Ge311	4 ×	2.5264(6)	2.5250(9)
Ge12	– Ge321	4 ×	2.1818(7)	2.183(1)
	– Ge322	4 ×	2.538(11)	2.547(11)
Ge21	– Ge322	3 ×	2.462(13)	2.462(13)
	– Ge21	1 ×	2.4736(6)	2.473(1)
	– Ge321	3 ×	2.5696(9)	2.569(1)
Ge22	– Ge322	1 ×	2.435(13)	2.419(13)
	– Ge22	1 ×	2.4438(6)	2.445(1)
	– Ge311	1 ×	2.5055(8)	2.504(1)
	– Ge311	1 ×	2.5094(8)	2.507(1)
	– Ge321	1 ×	2.5359(9)	2.538(1)
	– Ge312	1 ×	2.625(10)	2.632(12)
	– Ge312	1 ×	2.638(10)	2.642(12)
Ge311	– Ge322	1 ×	2.377(12)	2.382(12)
	– Ge22	1 ×	2.5055(8)	2.504(1)
	– Ge22	1 ×	2.5094(8)	2.507(1)
	– Ge11	1 ×	2.5264(6)	2.5250(9)
	– Ge11	1 ×	2.6098(9)	2.609(1)
Ge312	– Ge11	1 ×	2.143(10)	2.131(11)
	– Ge322	1 ×	2.619(15)	2.63(2)
	– Ge22	1 ×	2.625(10)	2.632(12)
	– Ge22	1 ×	2.638(10)	2.642(12)

	– Ge321	1 ×	2.818(10)	2.820(11)
Ge321	– Ge12	1 ×	2.1818(7)	2.183(1)
	– Ge22	1 ×	2.5359(9)	2.538(1)
	– Ge21	1 ×	2.5696(9)	2.569(1)
	– Ge311	1 ×	2.6098(9)	2.609(1)
	– Ge312	1 ×	2.818(10)	2.820(11)
Ge322	– Ge311	1 ×	2.377(12)	2.382(12)
	– Ge22	1 ×	2.435(13)	2.419(13)
	– Ge21	1 ×	2.462(13)	2.462(13)
	– Ge12	1 ×	2.538(11)	2.547(11)
	– Ge312	1 ×	2.619(15)	2.63(2)

Table 5: Lattice parameter and chemical compositions of $Ba_8Ge_{43}\square_3$

Material	Preparation route	Lattice parameter (Å)	Composition (WDXS)	Reference
	steel-quenched	21.3079(2)	$Ba_8Ge_{42.9(1)}$	This work
$Ba_8Ge_{43}\square_3$	steel-quenched	21.3062(2)	$Ba_8Ge_{43.0(1)}$	This work
	ann. at 790 °C for 1m	21.3069(3)	$Ba_8Ge_{43.0(1)}$	This work
$Ba_8Ge_{42}\square_4$	steel-quenched	21.3085(2)	$Ba_8Ge_{43.0(1)}$	This work
$Ba_8Ge_{44}\square_2$	steel-quenched	21.3066(2)	$Ba_8Ge_{43.0(1)}$	This work
$Ba_8Ge_{43}\square_3$	water-quenched	21.3123(6)	-	[14]
	ann. at 795 °C for 42d	21.3123(5)	-	[14]
	ann. at 790 °C for 12h	21.2748(2)	$Ba_8Ge_{42.9(1)}$	[16]

Figures

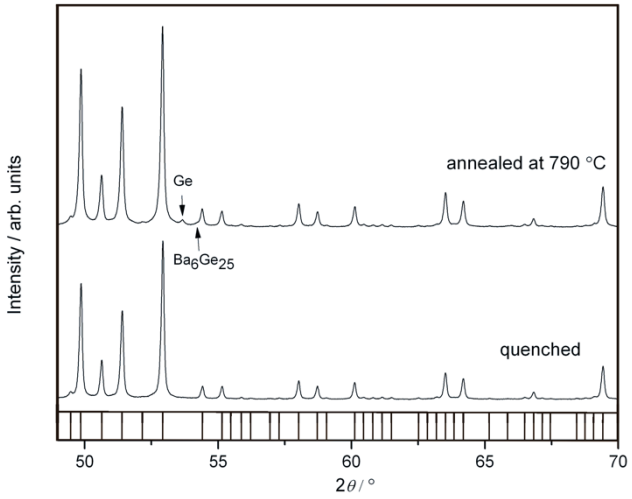

Fig. 1. XRPD patterns of $Ba_8Ge_{43}\square_3$ after quenching (bottom) and annealing (top). Ticks mark the calculated reflection positions. The quenched sample is a single phase, the annealed sample contains small amounts of α-Ge and Ba_6Ge_{25}. The half-width of the different peaks for both preparation routes is identical.

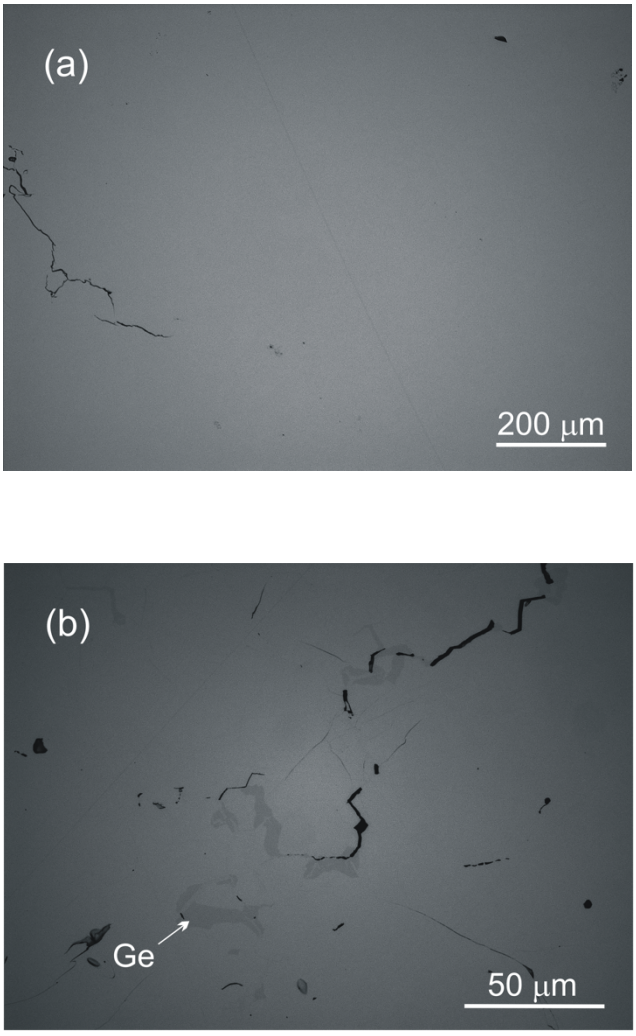

Fig. 2: Optical microscopy images of $Ba_8Ge_{43}\square_3$. (a) The quenched sample shows large areas without any detectable impurity. (b) Due to lower cooling rates the annealed sample contains α-Ge (marked) and small inclusions of Ba_6Ge_{25}.

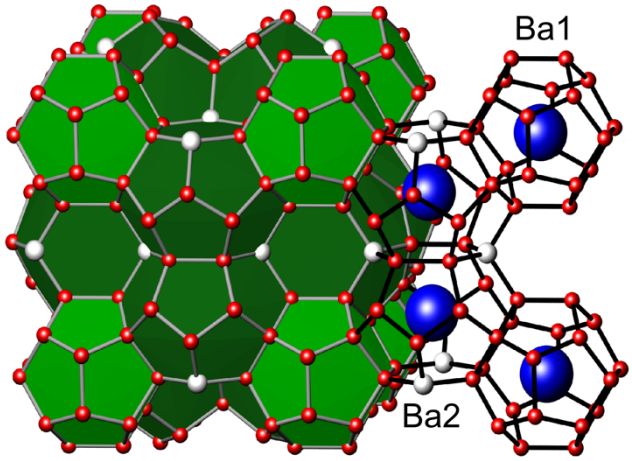

Fig. 3: The clathrate-I structure with possible defect positions (white spheres).

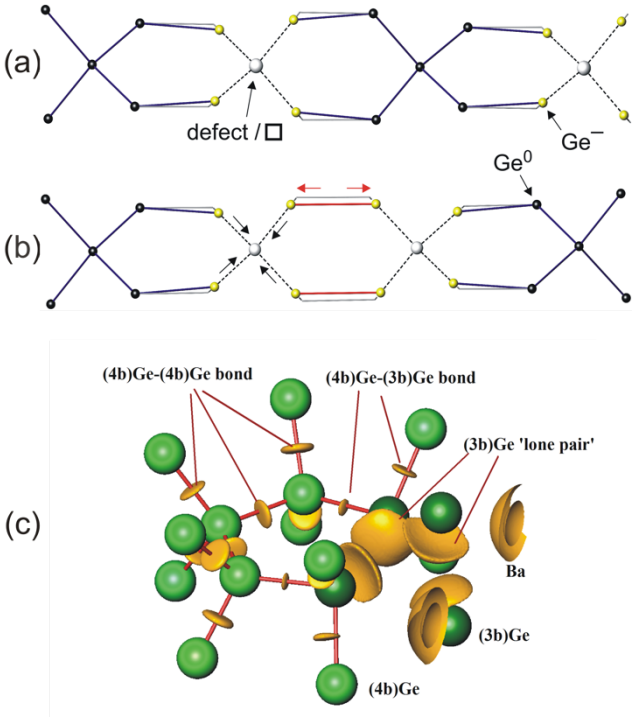

Fig. 4. Atomic arrangements and chemical bonding within the spiro-chain of hexagons in the crystal structure of $Ba_8Ge_{43}\square_3$: (a) defect-alternating and (b) defect-cumulating arrangement (c) Distribution of the electron localizability indicator in vicinity of the defect and the adjacent part of the chain. The positions of the ELI maxima reflecting the Ge-Ge bonds and the 'lone pairs' are visualized by the isosurfaces with $\Upsilon = 1.300$. The part of the outer core shells of the Ba atoms is shown on the right side.

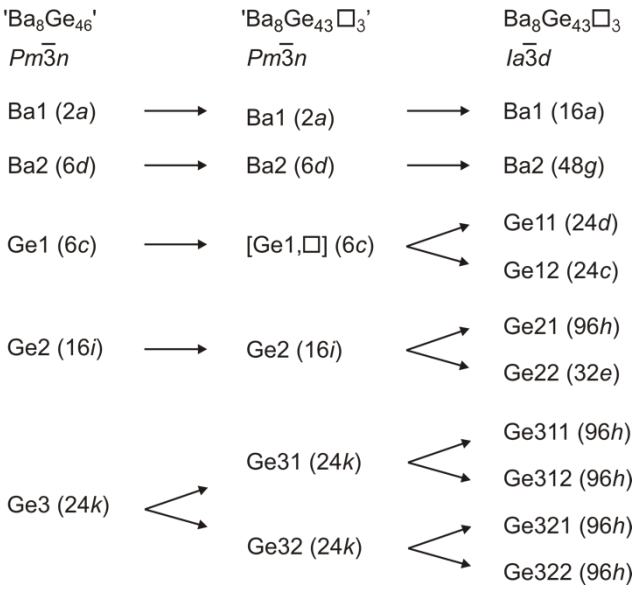

Fig. 5: Relation of Wyckoff sites between a clathrate free of defects ($Pm\bar{3}n$), with statistically distributed defects ($Pm\bar{3}n$) and ordered defect arrangement ($Ia\bar{3}d$).

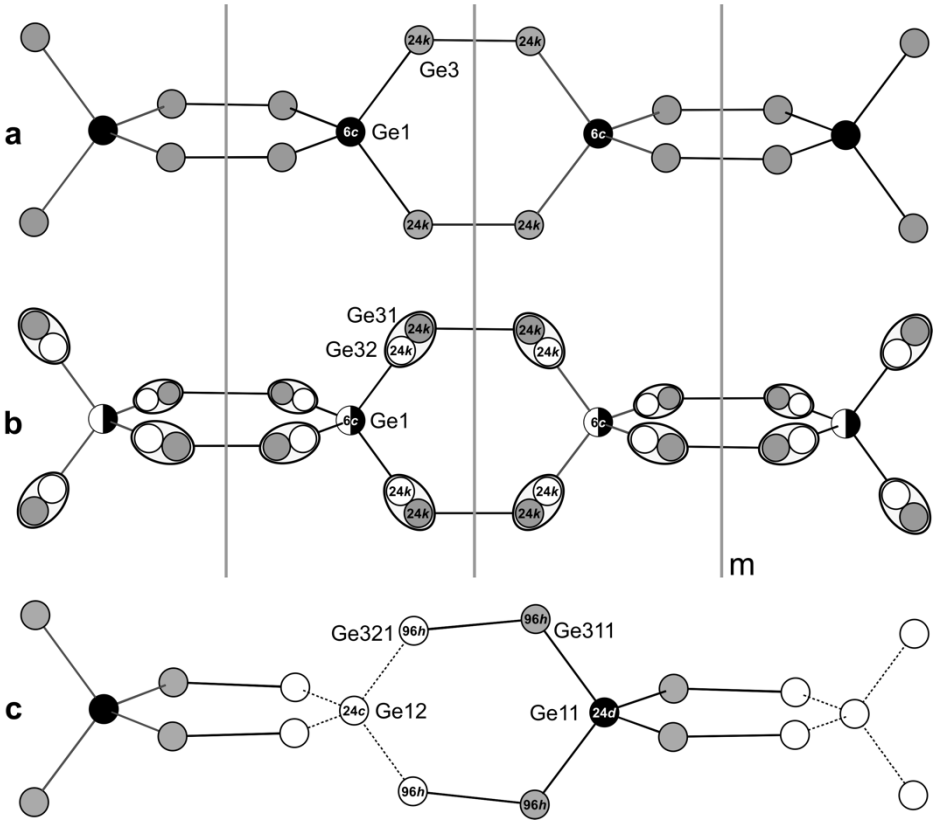

Fig. 6: Description of the defects within the spiro-chains of hexagons in the space groups $Pm\bar{3}n$ and $Ia\bar{3}d$. (a) defect free arrangement in $Pm\bar{3}n$, (b) split atom model of a defect clathrate in $Pm\bar{3}n$, (c) ordered defect arrangement in space group $Ia\bar{3}d$.

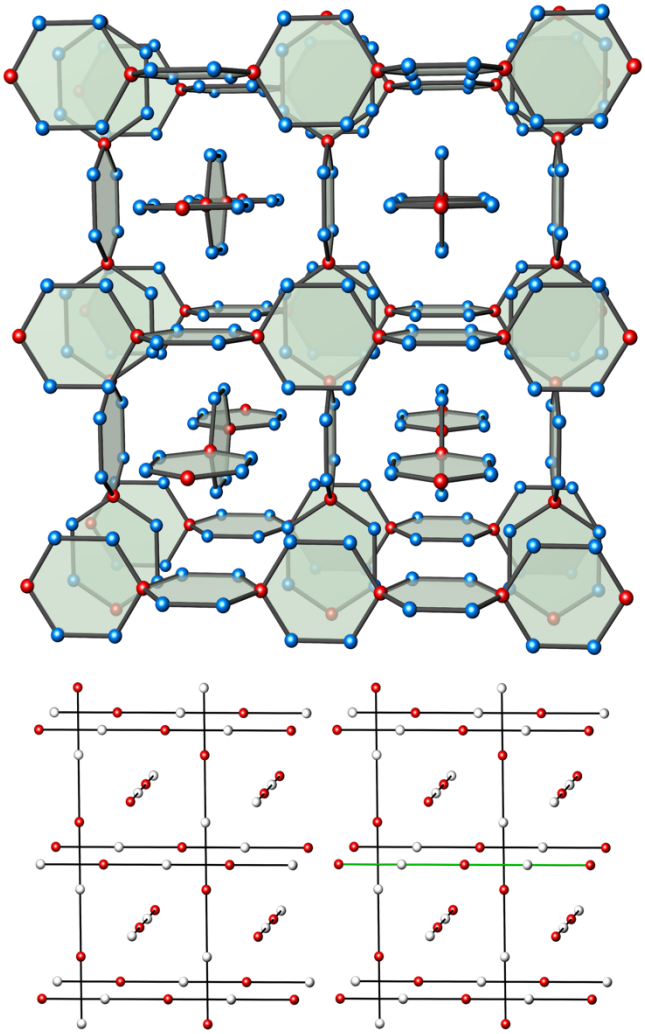

Fig. 7: (top) Spatial arrangement of the spiro-hexagon chains in the crystal structure of $Ba_8Ge_{43}\square_3$. (bottom) Possible defect arrangements within the chains with complete (left) or partial ordering (right). Model for partial ordering yields an occupancy of 8% for the Ge12 position as it is observed in the crystal structure refinement.

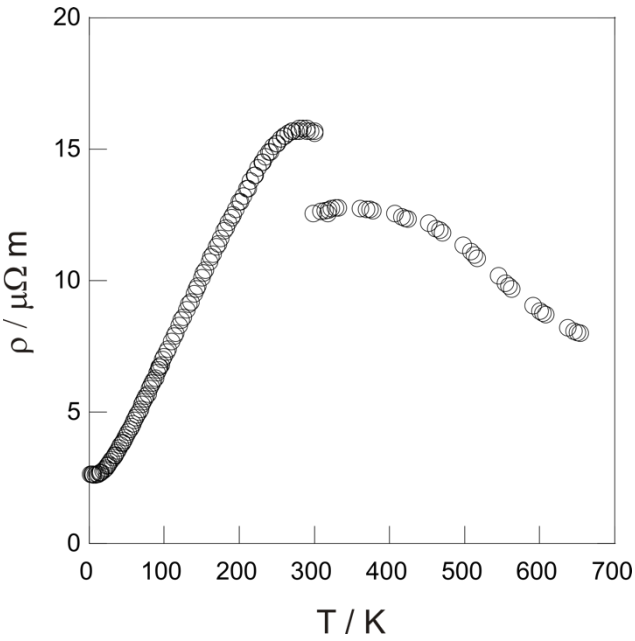

Fig. 8: Temperature dependence of the electrical resistivity of $Ba_8Ge_{43}\square_3$ in the temperature range 2 - 673 K. The shift at room temperature is caused by differences in the measurement setups for the low- and high-temperature ranges (cf. text)

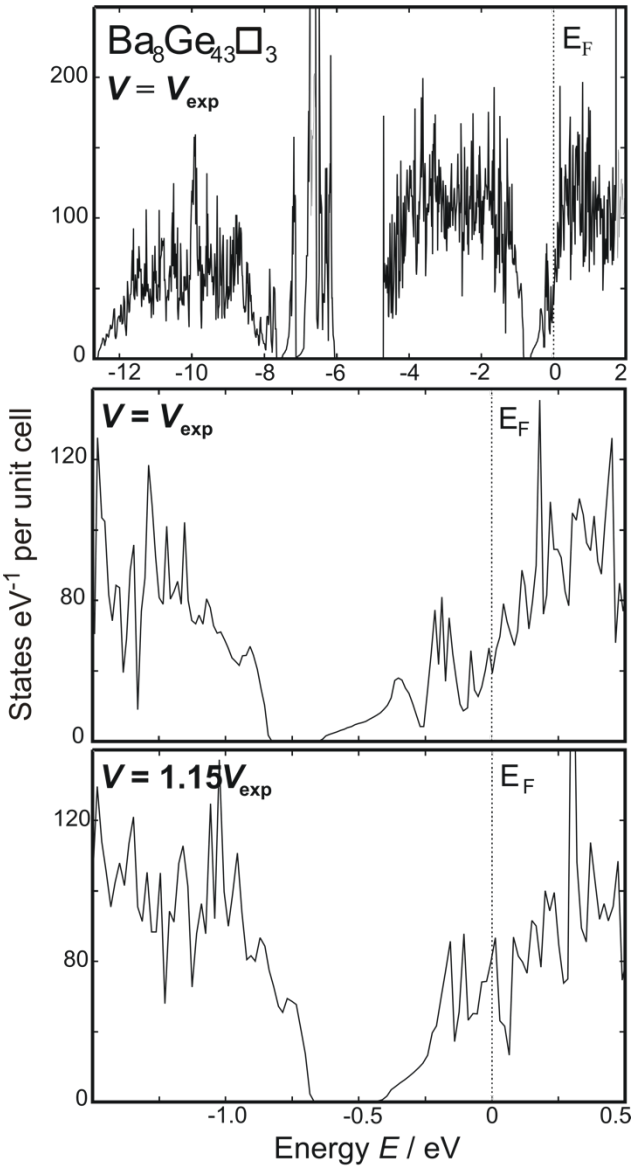

Fig. 9: Electronic density of states for an ordered model of $Ba_8Ge_{43}\square_3$ (cf. calculation procedure): (top) general view confirming occupancy of the antibonding states by excess electrons; (middle) energy region around the Fermi level as calculated for the experimentally observed unit cell volume; (bottom) energy region around the Fermi level as calculated for an enhanced volume modelling the temperature influence on DOS.

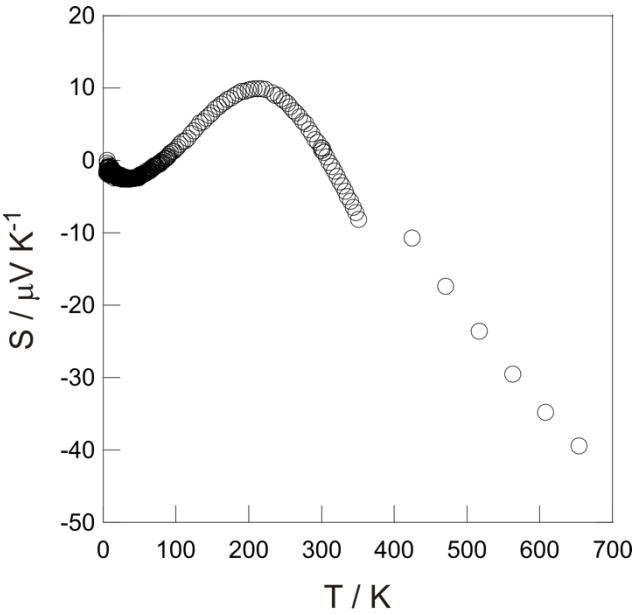

Figure 10: Temperature dependence of the thermopower $Ba_8Ge_{43}\square_3$ in the low and high temperature range.

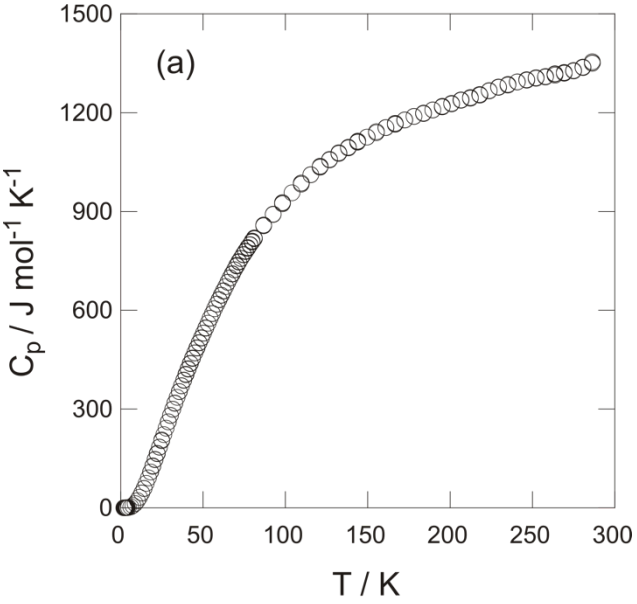
(a)
1500
1200
900
600
300
0
0
50
100
150
200
250
300
C_p / J mol^{-1} K^{-1}
T / K

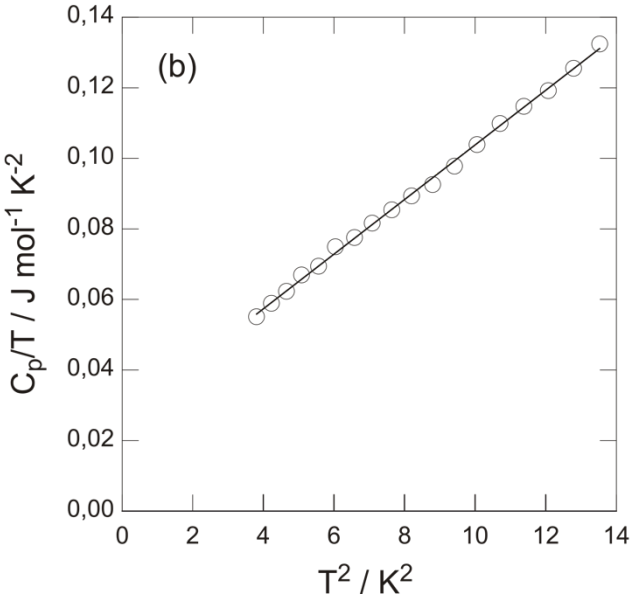
(b)
0,14
0,12
0,10
0,08
0,06
0,04
0,02
0,00
0
2
4
6
8
10
12
14
C_p/T / J mol^{-1} K^{-2}
T^2 / K^2

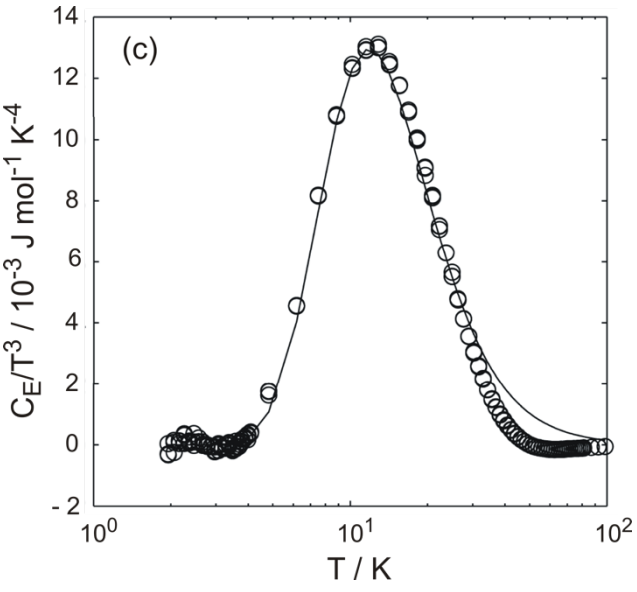
(c)
14
12
10
8
6
4
2
0
- 2
10^0
10^1
10^2
C_E/T^3 / 10^{-3} J mol^{-1} K^{-4}
T / K

Figure 11: Specific heat of $Ba_8Ge_{43}\square_3$: (a) low-temperature dependence of the specific heat C_p; (b) C_p/T plotted as a function of T^2 in the 2 - 3.5 K temperature range, the solid line stands for the best fit to the data according to the relation $C_p/T = \gamma + \beta T^2$; (c) Einstein contribution to the specific heat C_E plotted as C_E/T^3 vs T on a logarithmic scale, the solid line represents the best fit to the data.

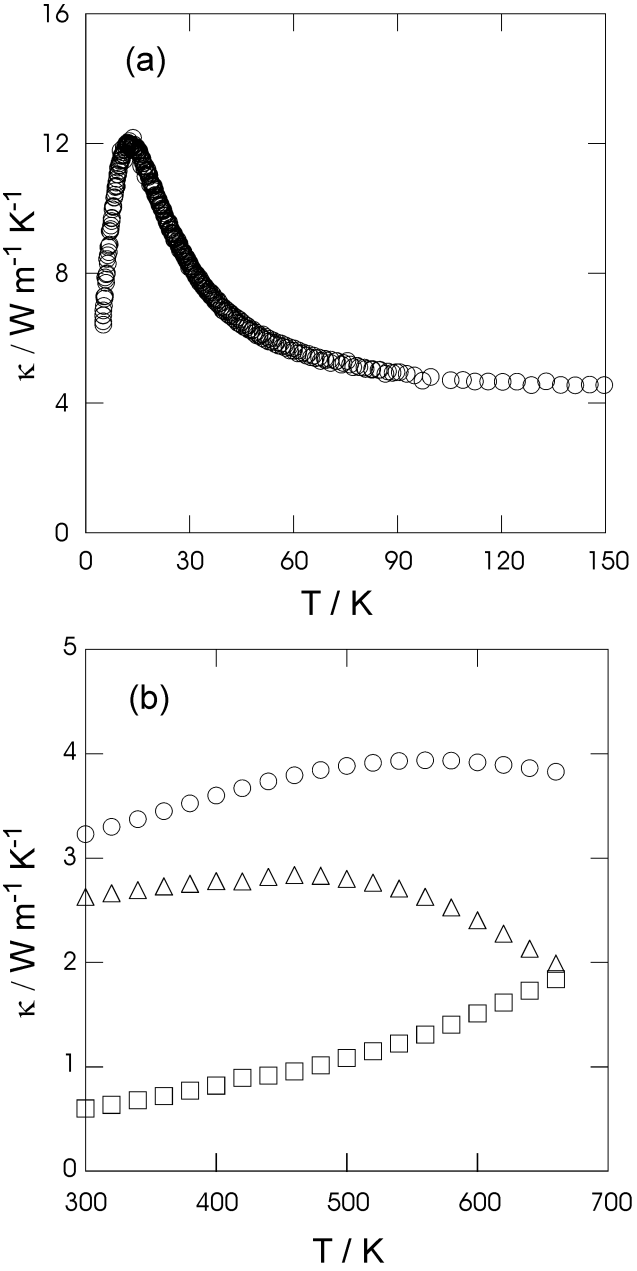

Figure 12: Thermal conductivity κ of $Ba_8Ge_{43}\square_3$: (a) temperature dependence of the total thermal conductivity in the low temperature range of 5 – 150 K. (b) high-temperature dependence of the total (°), electronic (□) and lattice (Δ) thermal conductivity.

References:

1 A. Saramat, G. Svensson, A. E. C. Pamqvist, C. Stiewe, E. Mueller, D. Platzek, S. G. K. Williams and D. M. Rowe, *J. Appl. Phys.*, 2006, **99**, 023708.

2 G. S. Nolas, T. J. R. Weakley, J. L. Cohn and R. Sharma, *Phys. Rev. B*, 2000, **61**, 3845-3850.

3 S. Yamanaka, H.-O. Horie, H. Nakano and M. Ishikawa, *Fullerene Sci. Tech.*, 1995, **3**, 21-28; H. Kawaji, K. Iwai, S. Yamanaka and M. Ishikawa, *Solid State Commun.*, 1996, **100**, 393- 395.

4 C. Cros and M.Pouchard, *C. R. Chimie*, 2009, **12**, 1014-1056; K. A. Kovnir and A. V. Shevelkov, *Russ. Chem. Rev.*, 2004, **73**, 923-938.

5 R. Kröner, K. Peters, H. G. von Schnering and R. Nesper, *Z. Kristallogr. NCS*, 1998, **213**, 667-668.

6 B. Eisenmann, H. Schäfer and R. Zagler, *J. Less-Common Met.*, 1986, **118**, 43-55; S. Paschen, W. Carrillo-Cabrera, A. Bentien, V. H. Tran, M. Baenitz, Yu. Grin and F. Steglich, *Phys. Rev. B*, 2001, **64** 214404.

7 V. Pacheco, A. Bentien, W. Carrillo-Cabrera, S. Paschen, F. Steglich and Yu. Grin, *Phys. Rev. B*, 2005, **71** 165205.

8 G. S. Nolas, J.-M. Ward, J. Gryko, L. Qiu and M. A. White, *Phys. Rev. B*, 2001, **64**, 153201.

9 A. Wosylus, I. Veremchuk, W. Schnelle, M. Baitinger, U. Schwarz, Y. Grin, *Chem. Eur. J.*, 2009, **17**, 2455-2458.

10 H. G. von Schnering, *Nova Acta Leopoldina*, 1985, **59**, 168-182; J. Llanos, *Dissertation*, Universität Stuttgart, 1984.

11 H. G. von Schnering, R. Kröner, M. Baitinger, K. Peters, R. Nesper and Y. Grin, *Z. Kristallogr. NCS*, 2000, 215, 205 - 206.

12 C. Cros, M. Pouchard and P. Hagenmuller, *J. Solid State Chem.*, 1970, **2**, 570-581.

13 W. Carrillo-Cabrera, J. Curda, K. Peters, S. Paschen, M. Baenitz, Y. Grin and H. G. von Schnering, *Z. Kristallogr. NCS*, 2000, **215**, 321-322.

14 W. Carrillo-Cabrera, S. Budnyk, Y. Prots and Yu. Grin, *Z. Anorg. Allg. Chem.*, 2004, **630**, 2267 - 2276.

15 N. L. Okamoto, M. W. Oh, T. Nishii, K. Tanaka and H. Inui, *J. Appl. Phys.*, 2006, **99**, 033513.

16 N. L. Okamoto, K. Tanaka and H. Inui, *Acta Mat.*, 2006, **54**, 173–178.

17 R. F. W. Herrmann, K. Tanigaki, T. Kawaguchi, S. Kuroshima and O. Zhou, *Phys. Rev. B*, 1999, **60**, 13245.

18 F. Dubois and T. F. Fässler, *J. Am. Chem. Soc.*, 2005, **127**, 3264-3265.

19 A. Kaltzoglou, S. D. Hoffmann and T. F. Fässler, *Eur. J. Inorg. Chem.*, 2007, 4162-4167

20 C. Candolfi, U. Aydemir, M. Baitinger, N. Oeschler, F. Steglich and Yu. Grin, Contribution presented at the 28th International Conference on Thermoelectrics, Freiburg, 2009.

21 http://www.cpfs.mpg.de/web/forschung/forschproj/eli/

22 O. Jepsen, A. Burkhardt and O. K. Andersen, Program TB-LMTO-ASA. version 4.7., Max-Planck-Institut für Festkörperforschung, Stuttgart, 1999.

23 U. von Barth and L. Hedin, *J. Phys. C*, 1972, **5**, 1629-1642.

24 O. K. Andersen, *Phys. Rev. B*, 1975, **12**, 3060-3083.

25 M. Kohout, *Int. J. Quantum Chem.*, 2004, **97**, 651-658.

26 M. Kohout, F. R. Wagner and Yu. Grin, *Int. J. Quantum Chem.*, 2006, **106**, 1499-1507; M. Kohout, *Faraday Disscuss.*, 2007, **135**, 43-54.

27 M. Kohout, Program Basin, version 4.3, 2008.

28 R. F. W. Bader, Atoms in Molecules: A Quantum Theory, Oxford University Press, Oxford, 1999.

29 L. T. K. Nguyen, U. Aydemir, M. Baitinger, E. Bauer, H. Borrmann, U. Burkhardt, J. Custers, A. Haghighirad, R. Höfler, K. D. Luther, F. Ritter, W. Assmus, Yu. Grin and S. Paschen, *Dalton Trans.*, this issue.

30 Y. Li, Y. Liu, N. Chen, G. Cao, Z. Feng and J. H. Ross Jr., *Phys. Lett. A*, 2005, **345**, 398-408.

31 S. Yamanaka, E. Enishi, H. Fukuoka and M. Yasukawa, *Inorg. Chem.*, 2000, **39**, 56-58.

32 K. Tanigaki, T. Shimizu, K. M. Itoh, J. Teraoka, Y. Moritomo and S. Yamanaka, *Nat. Mater.*, 2003, **2**, 653-655.

33 N. Melnychenko-Koblyuk, A. Grytsiv, P. Rogl, M. Rotter, R. Lackner, E. Bauer, L. Fornasari, F. Marabelli and G. Giester, *Phys. Rev. B*, 2007, **76**, 195124 and references therein.

34 S. Johnsen, A. Bentien, G. K. H. Madsen, M. Nygren and B. B. Iversen, *Phys. Rev. B*, 2007, **76**, 245126.

35 M. A. Avila, K. Suekuni, K. Umeo, H. Fukuoka, S. Yamanaka and T. Takabatake, *Phys. Rev. B*, 2006, **74**, 125109.

36 K. Suekuni, M. A. Avila, K. Umeo and T. Takabatake, *Phys. Rev. B*, 2007, **75**,195210.

37 H. Shimizu, T. Iitaka, T. Fukushima, T. Kume, S. Sasaki, N. Sata, Y. Ohishi, H. Fukuoka and S. Yamanaka, *J. Appl. Phys.*, 2007, **101**, 063549.

38 A. Bentien, M. Christensen, J. D. Bryan, A. Sanchez, S. Paschen, F. Steglich, G. D. Stucky and B. B. Iversen, *Phys. Rev. B*, 2004, **69**, 045107.

39 M. A. Avila, D. Huo, T. Sakata, K. Suekumi and T. Takabatake, *J. Phys.: Condens. Matter*, 2006, **18**, 1585.

40 B. C. Sales, B. C. Chakoumakos, R. Jin, J. R. Thompson and D. Mandrus, *Phys. Rev. B*, 2001, **63**, 245113.

To do:

- Change Figure (CC)
- Corrections (Prof. Steglich, Niels)
- Add comment to K8Ge44 Ramlau